Accurate isotopic fission yields of electromagnetically induced fission of ^{238}U measured in inverse kinematics at relativistic energies

E. Pellereau,[1,*] J. Taïeb,[1] A. Chatillon,[1,†] H. Alvarez-Pol,[2] L. Audouin,[3] Y. Ayyad,[2,‡] G. Bélier,[1] J. Benlliure,[2] G. Boutoux,[1,§] M. Caamaño,[2] E. Casarejos,[4] D. Cortina-Gil,[2] A. Ebran,[1] F. Farget,[5] B. Fernández-Domínguez,[2] T. Gorbinet,[1] L. Grente,[1] A. Heinz,[6] H. Johansson,[6] B. Jurado,[7] A. Kelić-Heil,[8] N. Kurz,[8] B. Laurent,[1] J.-F. Martin,[1] C. Nociforo,[8] C. Paradela,[2,‖] S. Pietri,[8] J. L. Rodríguez-Sánchez,[2,¶] K.-H. Schmidt,[8] H. Simon,[8] L. Tassan-Got,[3] J. Vargas,[2] B. Voss,[8] and H. Weick[8]

[1]*CEA, DAM, DIF, F-91297 Arpajon, France*

[2]*University of Santiago de Compostela, E-15782 Santiago de Compostela, Spain*

[3]*CNRS, IPN Orsay, F-91406 Orsay, France*

[4]*University of Vigo, E-36310 Vigo, Spain*

[5]*CNRS, GANIL, Boulevard H. Becquerel, 14076 Caen, France*

[6]*Chalmers University of Technology, 41296 Gothenburg, Sweden*

[7]*CNRS, CENBG, F-33175 Gradignan, France*

[8]*GSI-Helmholtzzentrum für Schwerionenforschung GmbH, D-64291 Darmstadt, Germany*

(Received 14 February 2017; published 3 May 2017)

SOFIA (Studies On Fission with Aladin) is a novel experimental program, dedicated to accurate measurements of fission-fragment isotopic yields. The setup allows us to fully identify, in nuclear charge and mass, both fission fragments in coincidence for the whole fission-fragment range. It was installed at the GSI facility (Darmstadt), to benefit from the relativistic heavy-ion beams available there, and thus to use inverse kinematics. This paper reports on fission yields obtained in electromagnetically induced fission of ^{238}U.

DOI: 10.1103/PhysRevC.95.054603

I. INTRODUCTION

The investigation of the properties of fission fragments has an important role in the nuclear-data field, for applications and for fundamental aspects. In particular, measurements of isotopic fission yields are relevant, not only as manifestation of underlying nuclear structure effects, which play a key role in low-energy fission, but also because those data are crucial for nuclear-reactor applications. Indeed, these isotopic fission yields, also defined as independent fission-product yields, are a key observable needed to predict the accumulation of long-lived fission products in reactor cores, the neutron flux, or the decay heat after a core shutdown. However, data on fission-fragment yields are still incomplete and often inaccurate. This lack of high-resolution data constitutes an obstacle for the development of predictive and reliable models. Even for the best-studied fission reaction, i.e., thermal-neutron-induced fission of ^{235}U, in the evaluated libraries, uncertainties associated with isotopic fission yields [1] are below 10% in some cases (such as some Kr, Rb, Sr, Mo, Sn, or Xe isotopes) and above 30% in many more.

In standard experiments, where a neutron, light charged particle, or γ ray impinges on an actinide target at rest in the laboratory frame, fission fragments are identified in flight by measuring their energies and/or times of flight. In this so-called direct kinematics method, the fission fragments have the kinetic energy they get from the fission process. While measuring the energies, experimental constraints prevent from getting an unambiguous measurement of the nuclear mass and charge of the fission fragments, especially for the heavy ones. Indeed, due to the strong fluctuation of ionic charge states, a clear assignment of the atomic number has only been achieved for light fragments [2–4]. Moreover, the kinetic energy measurement of the fission fragments is deteriorated, first, by the energy loss in the target and, second, by the energy spread due to the neutron emission. When the times of flight of the fission fragments are measured, the mass prior to neutron evaporation can be reconstructed, since the prompt neutron emission only broadens the velocity distribution, but does not change its mean value. However, this advantage is counterbalanced by the limited time-of-flight resolution. Nowadays, new detection systems such as SPIDER [5], VERDI [6], and FALSTAFF [7] are being developed, pushing further the detection technology, based on the combination of the energy and time-of-flight measurements, as previously used in the Cosi Fan Tutte experiment [8]. With the advent of electromagnetic spectrometers, such as Lohengrin [9] or Hiawatha [10], high-resolution data on isobaric yields can be measured with an uncertainty below 5%, while isotopic identification is still limited to the light fission fragment group; see for example Ref. [11]. An exception are experiments that measure in addition β-delayed γ rays [12], which allows measurement of a few isotopic yields. However, with this technique results on isotopic yields remain partial.

[*]Present address: UMR CNRS UVSQ 8180, ILV, 45 Avenue des États-Unis, F-78035 Versailles, France.

[†]audrey.chatillon@cea.fr

[‡]Present address: National Superconducting Cyclotron Laboratory, Michigan State University, East Lansing, MI 48824-1321, USA.

[§]Present address: Centre Lasers Intenses et Applications, Université Bordeaux1, 351 Cours de la Libération, 33405 Talence, France.

[‖]Present address: EC-JRC, Institute for Reference Materials and Measurements, Retieseweg 111, B-2440 Geel, Belgium.

[¶]Present address: IRFU, CEA, Université Paris-Saclay, F-91191 Gif-sur-Yvette, France.

To overcome those experimental constraints in direct kinematics, alternative approaches based on the use of inverse kinematics coupled with a magnetic spectrometer have been developed. That new generation of experiments, initiated at GSI (Darmstadt) by Armbruster, Schmidt, and collaborators [13–15], enables to take a step forward in fission studies. These approaches are briefly presented in Sec. II A. The SOFIA (Studies On Fission with Aladin) experiment is based on this method, using relativistic beams. At such high energies, Coulomb excitation (Sec. II B) is the most suitable reaction mechanism to excite nuclei in flight and study their low-energy fission. The experimental setup and analysis procedure are presented in Secs. II D and III, followed by the results on fission yields (Sec. IV) obtained for the fission of ^{238}U.

II. EXPERIMENTAL SETUP

A. Inverse kinematics at relativistic energy

In inverse kinematics, actinides are accelerated, and the fissioning systems are produced using surrogate reactions. Thanks to the kinematic boost, fission fragments are emitted at forward angles with higher recoil energies, and their elemental distribution can be measured with improved resolution. Using this technique, isotopic yields can be measured even for the heavy fission fragments.

At GANIL (Grand Accélérateur National d'Ions Lourds), inverse kinematics is used to produce fissioning nuclei by transfer or fusion reactions of a ^{238}U beam at 6A MeV on a ^{12}C target [16,17]. At GSI, where the SOFIA experiment takes place, experiments can benefit from beams at relativistic energies, which allow unambiguous identification of nuclear charge over the whole fission-fragment range. At such high energies, ions are fully stripped, thus the ionic charge obtained by energy-loss (ΔE) measurements gives direct information on the nuclear charge ($\Delta E \propto Z^2$). The main difficulty with this approach lies in the measurement of the mass number, since it requires a large-scale detection system to combine the energy-loss measurement of a heavy ion with its time-of-flight (ToF) and its magnetic rigidity ($B\rho$). With these three observables, the mass A of the ion can be deduced using the so-called $B\rho$-ΔE-ToF method.

This method was already applied in the 1990s at the fragment separator (FRS [18]) of the GSI facility, for two types of fission experiments. First, a primary ^{238}U beam at 750A MeV, impinging on a Pb target, was used [13]. Only one fragment per event, produced either by fission or fragmentation reactions, was isotopically identified using the FRS, which has an angular acceptance of $\pm$15 mrad. However, the transmission of the FRS is limited to a longitudinal momentum range of $\pm$2%. In this case, the low-energy fission component is extracted from the measured $B\rho$ distribution. Our experimental results will be compared to results obtained in a previous experiment [19] based on this method. In a second type of experiment, the FRS was used to produce separated and, on an event-by-event basis, identified secondary radioactive actinide beams. Fission of those radioactive beams was induced at the final focal plane of the FRS by Coulomb excitation, and both fission-fragment charges were measured in coincidence with a good resolution over the whole fragment range [14,15]; however, it was not possible to measure the masses of the fission fragments.

SOFIA builds on the experience gained in these previous GSI experiments, in order to obtain the isotopic identification of both fission fragments in coincidence for several fissioning actinide and pre-actinide nuclei. This article will focus on results obtained for electromagnetic fission of a relativistic primary ^{238}U beam, during the first experiment carried out in 2012.

B. Electromagnetically induced fission

In order to study low-energy fission of a relativistic beam, Coulomb excitation is the most favorable excitation mechanism. It populates mainly the isovector giant dipole resonances (IVGDR) with one or two phonons, as well as the isoscalar and isovector giant quadrupole resonances (ISGQR and IVGQR). After excitation, ^{238}U may deexcite through fission. Details of the reaction process are discussed in Ref. [15]. In the following, a brief summary is given for the experimental conditions of this work (^{238}U at 650A MeV impinging on a ^{238}U target). It is illustrated using calculated cross sections and excitation energies, since they cannot be measured. Compared to Ref. [15], the electromagnetic cross sections are calculated using the giant resonance parameters corrected with the values given in Ref. [20].

The total electromagnetic cross section [full red line in Fig. 1(a)] peaks around a mean excitation energy value of 12.2 MeV, with a tail up to 30 MeV. The calculation includes the main contribution of the GDRs and the GQRs, represented by the dashed blue line and the purple dotted line, respectively. Above the fission barrier at 5.8 MeV in ^{238}U, the electromagnetically excited ^{238}U nucleus may deexcite by fission with a cross section of about 2 b, obtained from the fission probability given in Fig. 1(b), which was calculated by the TALYS code [21]. The excitation function of the fissioning system is represented in Fig. 1(c). The mean excitation energy of the ^{238}U fissioning nucleus is 14.7 MeV, while the entire distribution is relatively broad. Therefore, for energies above S_{xn} [the neutron(s) separation energy(ies)], higher-chance fission becomes possible. The probabilities for the first and higher-chance fission channels are given in Table I. Those values were obtained using the general fission model (GEF, version 2015-2.2 [22]), with the calculated excitation function set as input.

Finally, studying the electromagnetically induced fission of ^{238}U is equivalent to studying the fission of ^{237}U induced by a neutron that leads to a compound nucleus excited at 14.7 MeV on average.

C. Fission-reaction detection

Depending on the nuclear charge of the target and on the impact parameter, different reaction channels are open: nuclear reactions (for impact parameters smaller than the sum of the radii of projectile and target) and Coulomb excitation (for high-Z targets and larger impact parameters). To favor Coulomb excitation, high-Z targets are needed. Therefore, two 600 μm thick uranium targets and one 125 μm thick lead target were

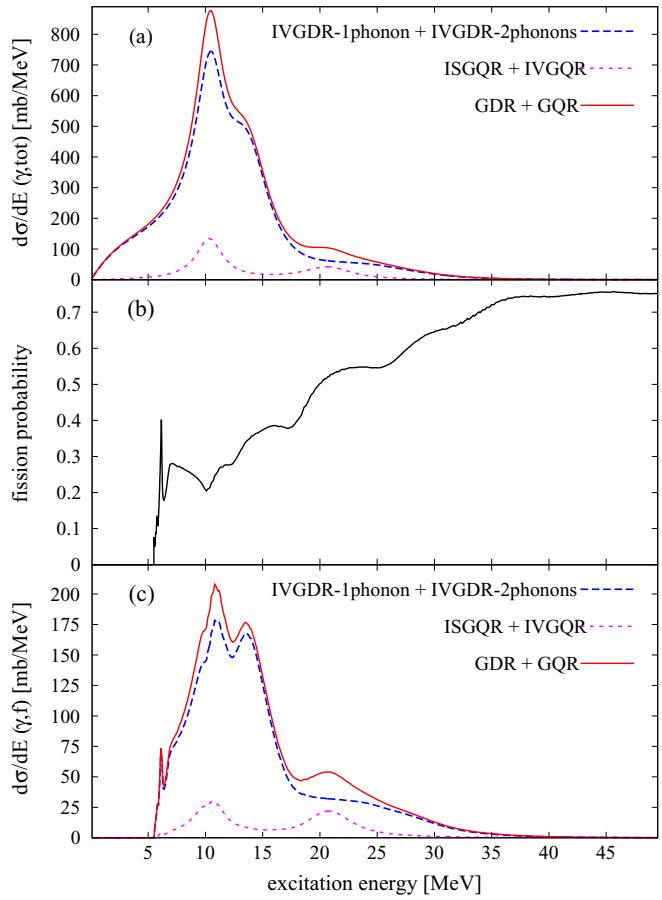

FIG. 1. (a) Total electromagnetic differential cross section, as function of the excitation energy of the compound nucleus, calculated for a ^{238}U projectile at 650A MeV on a ^{238}U target. (b) Fission probability of the compound nucleus ^{238}U calculated by TALYS. (c) Calculated excitation function for electromagnetically induced fission of ^{238}U.

mounted as cathodes in an active target filled by P10 gas, whereas the anodes were made of 18 μm thick aluminum foils (Fig. 2).

This active target is a stack of ionization chambers, each part measuring the energy loss of the ions in the respective section. As previously mentioned, $\Delta E \propto Z^2$; therefore, in first approximation, the nuclear charge of a fission fragment is equal to half of the nuclear charge of the compound nucleus, giving $\Delta E_{CN} = 2 * \Delta E_{FF1+FF2}$, where ΔE_{CN} stands for the energy loss by the compound nucleus and $\Delta E_{FF1+FF2}$ for the sum

TABLE I. Probabilities for higher-chance fission occurring in electromagnetically induced fission of ^{238}U, taking into account the excitation function given in Fig. 1(c).

Fission chance	Probability (%)
^{238}U(γ, f)	75.6
^{238}U$(n\gamma, f)$	15.6
^{238}U$(2n\gamma, f)$	7.7
^{238}U$(3n\gamma, f)$	1.0

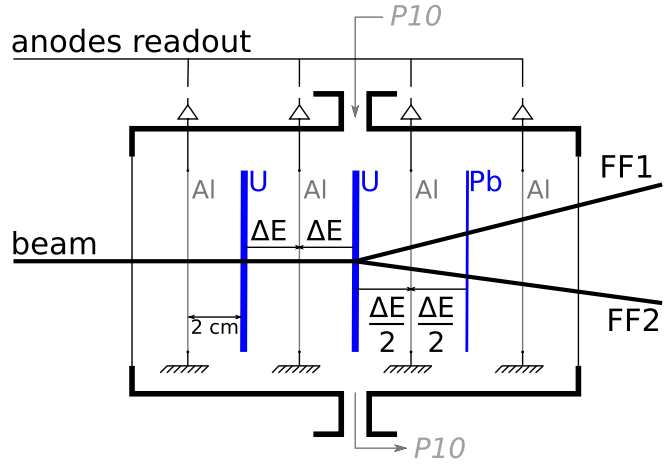

FIG. 2. Schematic view of the active target. Uranium and lead targets mounted as cathodes are biased at −280 V. Aluminum anodes are grounded and connected to preamplifiers for readout. Energy losses and expected signals for the second and third anodes are indicated in the case of fission occurring in the second cathode. ΔE, here, stands for the energy loss of the fissioning nucleus in one section of the active target.

of the energy losses by the fission fragments. Since the total ionisation energy of both fission fragments is approximately half of that of the fissioning secondary beam, the correlation of two neighboring sections provides us with information on the location of the fission event (Figs. 2 and 3). In this way we discriminate fission events taking place in the targets from those occurring in the layers of matter placed before or after the targets.

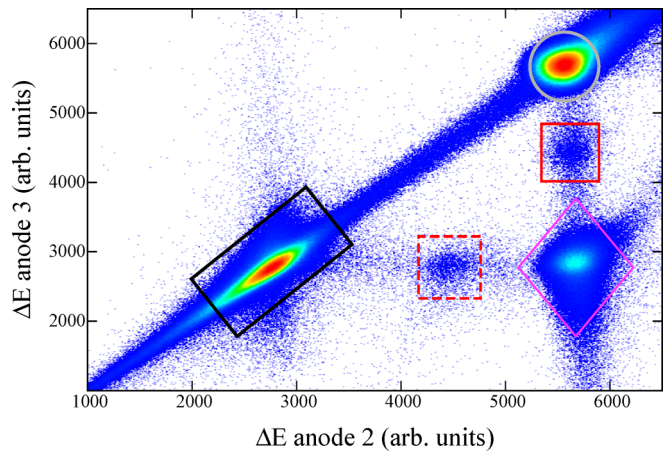

FIG. 3. Energy loss $\Delta E_{\text{anode-3}}$ versus $\Delta E_{\text{anode-2}}$. Grey circle: primary beam events characterized by maximized and similar energy losses measured by both anodes. Black rectangle: fission events occurring before anode 2. Fragmentation events are located along the diagonal. Red squares: fission in anode 2 (dashed line) and anode 3 (full line). Pink diamond: fission events in the second uranium cathode, as represented in Fig. 2.

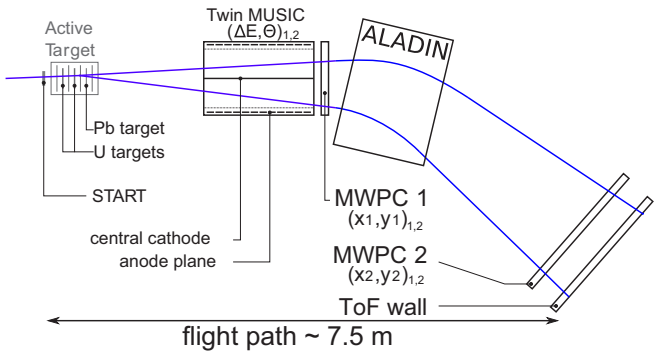

FIG. 4. Schematic view of the SOFIA setup to identify the nuclear mass and charge of both fission fragments in coincidence (top view, not on scale).

D. Fission-fragment identification

The SOFIA experimental setup (Fig. 4) was conceived to match the already existing ALADIN (A Large Acceptance DIpole magNet [23]) magnet, located at cave C at GSI, which is essential to measure the nuclear masses of the fission fragments.

Both fission fragments are, due to their Lorentz boost, focused in the forward direction and pass through Twin-MUSIC, made of two identical MUSICs (multiple sampling ionization chambers [24]) with a common vertical cathode, as shown in Fig. 5. Each MUSIC has a segmented anode plane dividing it into 10 vertical anodes along the path of the ions, in order to provide for each fission fragment its nuclear charge from the energy-loss signals and its horizontal angle [with a resolution of 0.8 mrad full width half maximum (FWHM)] from the electron drift times.

To complete the tracking, two MWPC (multiwire proportional chamber) detectors [25] located up- and downstream from ALADIN give the (x,y) position coordinates, with a resolution (FWHM) of 200 μm in the horizontal direction for the first MWPC, of 300 μm for the second MWPC, and of 1.5 mm in the vertical direction for both detectors. Finally, the time of flight of each fragment is measured with a resolution of 40 ps (FWHM) on a flight path of 7.5 m, between the START plastic scintillator located prior to the active target, and the time-of-flight wall [26]. The dimensions of all detectors were

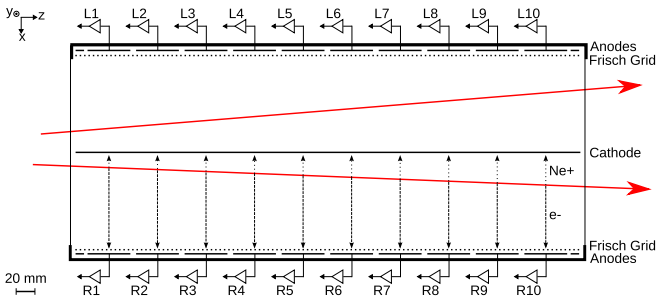

FIG. 5. Schematic top view of the Twin-MUSIC. Full line arrows: trajectories of the fission fragments. Dashed line arrows: drift of the electrons towards the anode plane. Dotted line arrows: drift of ions towards the cathode.

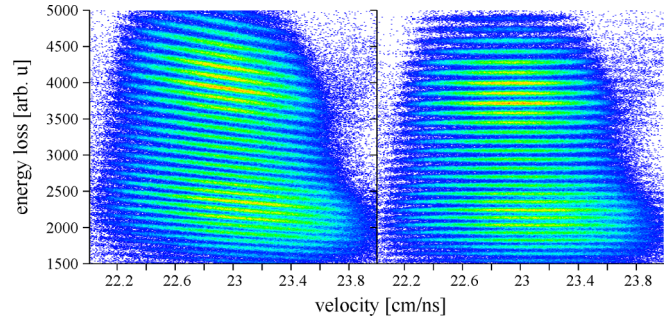

FIG. 6. Raw energy loss of fission fragments measured in the Twin-MUSIC as a function of their velocity, before (left) and after correction (right).

chosen to match the emission angle of the fission fragments (40 mrad).

III. DATA ANALYSIS

A. Elemental distribution

The first step of the analysis is to reconstruct the nuclear charges of both fission fragments for each event in coincidence. The two segmented anode planes of the Twin-MUSIC, provide a set of ten independent energy-loss measurements for each fragment. Only data from the eight central anodes are averaged to calculate the energy loss for a given fragment, since the signals from the outer anodes suffer from inhomogeneities in the electric field.

The reconstructed energy loss exhibits some dependencies. The most important is the dependence on the velocity of the fragments (Fig. 6). It arises mainly from the emission angle of the fission fragments in the center-of-mass frame. The fragments emitted in forward direction have a higher velocity in the laboratory frame than those emitted backwards. A correction is therefore applied to remove this dependence. Moreover, an additional correction related to the horizontal position of the fission fragment is applied to compensate for the charge recombinations due to the non-negligible attachment coefficient of the gas mixture (composed of Ne at 84.7%, CH_4 at 12%, CO_2 at 3%, and N_2 at 0.3%). Figure 7 shows the nuclear charges of the two fragments, passing the Twin-MUSIC on the respective sides of the cathode, plotted versus each other. The resolution reached is 0.4 charge units (FWHM) for all fission fragments.

B. Subtraction of fragmentation-fission events

Figure 7 presents the correlation of the nuclear charges of both fission fragments from events occurring in the uranium and lead targets. Maxima along several lines indicate different values of $Z_{\rm sum}$ (inset of Fig. 7), defined as the sum of the nuclear charges of both fission fragments.

Since the fission fragments are neutron rich and their excitation energy is in general too low to lead to proton evaporation, $Z_{\rm sum}$ gives the charge of the fissioning nucleus. The different values of $Z_{\rm sum}$ indicate different reaction mechanisms. For $Z_{\rm sum} = 93$, a charge-exchange reaction of ^{238}U takes place inside the target, which is followed by fission, while $Z_{\rm sum} < 92$

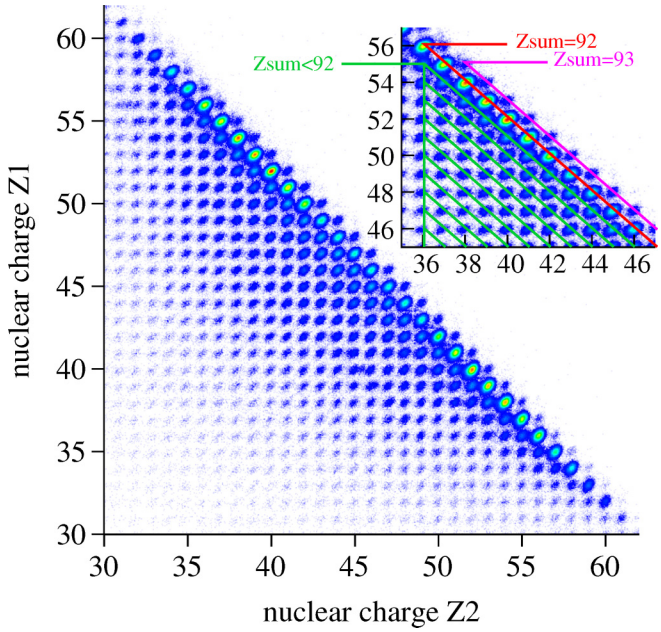

FIG. 7. Calibrated charge of the two correlated fission fragments. The resolution allows to select events that fulfill the condition $Z_{\rm sum} = 92$ unambiguously. In the inset, lines illustrate different values for $Z_{\rm sum}$, the sum of the charges of the two fission fragments.

corresponds to different fragmentation-fission channels, where the ^{238}U beam loses some protons in a nuclear collision prior to fission. Finally, $Z_{\rm sum} = 92$ is a sum of two fission processes: fragmentation fission, where only neutrons are removed in the fragmentation stage, and, electromagnetically induced fission, which is the reaction channel we want to study and select.

In order to eliminate the major part of the fragmentation-fission events, a first selection is made by keeping only events that fulfill the condition $Z_{\rm sum} = 92$. Such a spectrum still contains a minor contribution of fission events caused by fragmentation fission, in which only neutrons are removed during the fragmentation phase. Our experimental setup does not allow us to disentangle these two components on an event-by-event basis. Nevertheless, it is possible to subtract the corresponding proportion of fragmentation-fission events by exploiting the limiting fragmentation hypothesis [27]: for fragmentation reactions, the distributions in nuclear charge, mass, and excitation energy are independent of target and beam energy. To obtain events that originate only from fragmentation fission, we use events where fission occurred in one of the aluminum anodes of the active target or in the glass exit window of an FRS MUSIC detector (some 60 cm upstream the active target, not represented in Fig. 4). In such low-Z materials (aluminum, silicon, oxygen) mostly fragmentation-fission can occur, the Coulomb excitation cross section being of tens of mb only. Once scaled accordingly, their charge yields can be subtracted from the charge yields obtained in uranium and lead targets, after the selection $Z_{\rm sum} = 92$.

The subtraction procedure is illustrated in Fig. 8, while the results are presented in Fig. 9. The charge-sum spectra are measured for fission events in the cathodes of the active target (long-dashed blue line in Fig. 8), and for fission

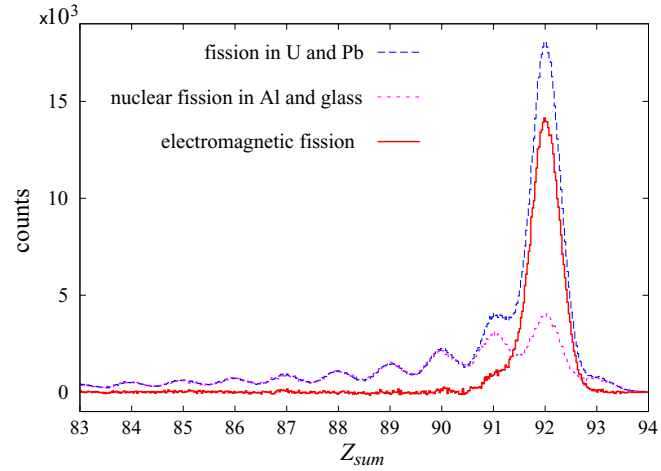

FIG. 8. Charge-sum spectra of the two fragments for different targets. The dashed blue line shows the spectrum measured from fission events occurring in the uranium and lead cathodes of the active target, while the pink dashed line represents fission events in the aluminum anodes of the active target and the exit glass window of an FRS MUSIC (not represented in Fig. 4). The latter spectrum has been properly scaled. The remaining spectrum after subtraction, i.e., the electromagnetic component, is shown as full red line.

occurring in the aluminum of the active target and in glass. The latter spectrum is scaled (small-dashed pink line in Fig. 8) by a factor obtained so that the yields from $Z_{\rm sum}$

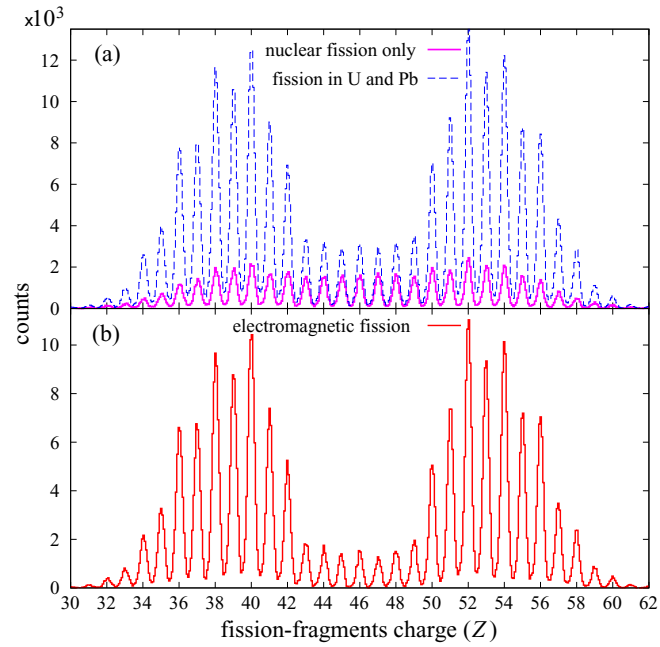

FIG. 9. Elemental distributions for fission of ^{238}U in different targets requiring $Z_{\rm sum} = 92$. (a) The dashed blue line represents the spectrum measured from fission events in uranium and lead targets, while the thick pink line is the charge distribution of fission fragments from fission events in aluminum anodes of the active target and the glass exit window of an FRS MUSIC detector. (b) The spectrum after subtraction, i.e., the electromagnetic component, is shown in red.

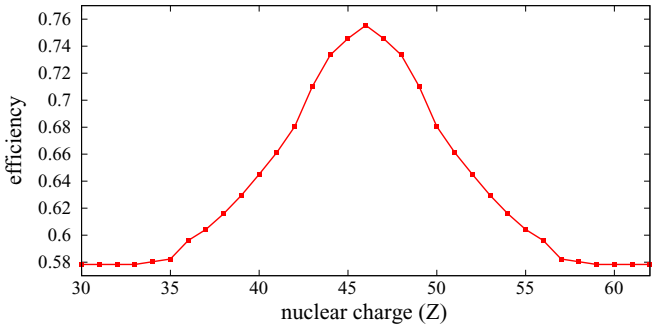

FIG. 10. Efficiency as a function of the nuclear charge of the fission fragments of the SOFIA detection system as set up in the 2012 experiment.

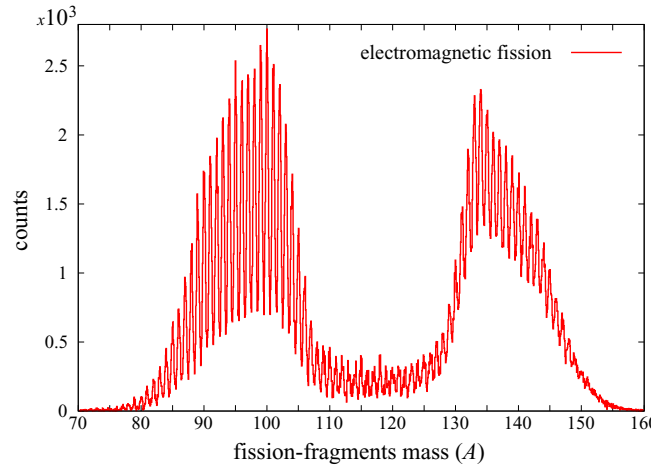

FIG. 11. Fission-fragment mass distribution for electromagnetically induced fission of ^{238}U.

equal to 85 up to 90 match the corresponding yields of the same spectra for fission induced in the three cathodes. The spectrum resulting from the subtraction (full red line in Fig. 8) corresponds to the electromagnetically induced fission component, which exhibits a single peak at $Z_{\mathrm{sum}} = 92$. The total disappearance of the other peaks proves the quality of such a subtraction and validates the limiting fragmentation hypothesis. Approximately 20% of fragmentation events still preserve a charge sum equal to 92. Then, the elemental distribution from fission events in the anodes is scaled with the same factor [pink thick line spectrum in Fig. 9(a)] and subtracted from those originating from the cathodes [dashed blue line spectrum in Fig. 9(a)], both requiring $Z_{\mathrm{sum}} = 92$. The spectrum in Fig. 9(b) shows the fission-fragment nuclear-charge distribution, for electromagnetically induced fission only, from which elemental yields are extracted.

C. Efficiency correction

The elemental yields need to be corrected for the detection efficiency of the setup, which was calculated, by a full Monte Carlo simulation, to be 63% and depends on the nuclear charge of the fission fragments, as shown in Fig. 10. Indeed, three sources of efficiency loss were identified. First, events where both fission fragments were passing through the same half of the Twin-MUSIC are lost because they cannot be discriminated. Second, when the fragments were crossing the central cathode, the number of usable anodes was too small to preserve a good charge resolution, so those events were eliminated from the analysis. Finally, the plastic scintillators, which were used in the time-of-flight wall, exhibited a light attenuation length that was shorter than expected, and some photomultiplier tubes (PMTs) had a lower nominal high-voltage value. As a consequence, events characterized by a very asymmetric fission with a light fragment hitting the edge of the plastic were partially lost.

A set of simulations were done (with the same cuts applied in the analysis) to reproduce the experimental fragment distribution at the MWPC2 plane, 46 cm upstream from the time-of-flight wall, and thus to measure and quantify those losses. Whereas the first two sources cause no problem, because they only induce a loss of statistics, the third source is biasing the data. This latter was integrated into the efficiency calculation, using the codes CONFID [28], to simulate the setup, and GEF [22], as event generator. The correction factor depending on the charge asymmetry could therefore be obtained.

Despite the moderate thickness of the targets, more than one reaction can occur in the targets. Those multi-reaction events are mostly removed while applying the $Z_{\mathrm{sum}} = 92$ condition. The remaining part leading to Z_{sum} equal to 92, which cannot be experimentally discriminated, was estimated to represent 1% of the total statistics. These multireactions are due to fragmentation reactions, either on the ^{238}U beam prior to fission (leading to fission of $^{238-xn}$U), or on fission fragments. The subtraction of this contribution was not included in this yields analysis but is reflected in the systematic uncertainties.

D. Mass distribution

When the charge, bending radius, and velocity of the fission fragments are extracted accurately, the mass is obtained from $A/Z \propto B\rho/(\beta\gamma)$, resulting in the mass spectrum presented in Fig. 11.

The mass-number calibration was obtained using the mass numbers determined in inverse kinematics for ^{238}U in a previous experiment [19]. The nuclear contribution is subtracted to extract the low-energy fission component of the mass yields. The same weight of the nuclear contribution as the one calculated in the nuclear-charge analysis is applied to the mass distribution obtained for fission occurring in the low-Z material. Finally, the efficiency correction is applied following the same protocol as the one described above for the elemental yields.

The mass distribution (Fig. 11) was measured with an outstanding resolution of 0.6 units (FWHM) in the light fragment group and 0.8 units (FWHM) in the heavy fragment group. Such results are due to the remarkable resolution obtained in time and position thanks to this new setup.

IV. RESULTS

All results with their statistical uncertainties are given in Tables IV to VII in the Appendix. Nonstatistical uncertainties need to be added. These take into account the nuclear-subtraction contribution, the efficiency correction, and the multireactions contribution. They were estimated, for elemental, isotonic, and mass yields, to be 0.5% for the most populated asymmetric split and 1% in the symmetric region, whereas for isotopic yields they were 0.5% and 2%. The difference in these uncertainties mainly comes from the nuclear subtraction weight.

In the following, the experimental results of this work will be presented and compared to data from Ref. [19], to calculated results from version 2015-2.2 of the GEF code [22], and to evaluated data from JEFF.3.1 [29,30] and ENDF-BVII.1 [31].

GEF is a semiempirical model. It is based on the observation of a common, general behavior of the fission properties of a broad variety of fissioning nuclei that is traced back to well-founded theoretical ideas. The physics behind GEF is described in Ref. [22]. This theoretical frame establishes links between different fission observables of different fissioning systems. In this article, it is used with the excitation distribution presented in Fig. 1(c) set as input for electromagnetically induced fission of ^{238}U. All our measured fission observables are available as outputs in the GEF code, for the same fissioning system, and thus can be compared. Such a comparison, with our new data, would help to test the validity of the above-mentioned links and systematic trends of the fission quantities.

As for the evaluated data, the comparison is done with yields from ^{238}U(n,f) reactions, since ^{237}U(n,f) has never been studied experimentally because of the short half-life of ^{237}U.

A. Elemental yields and even-odd staggering

In order to obtain the elemental yields, the elemental distribution spectrum [Fig. 9(b)] is integrated using a multi-Gaussian fit, and the sum of all peaks is normalized to 200%. The result is presented in Fig. 12 (full red line). There is a global enhancement of the even charges ($Y_{\rm even}$) compared to their odd neighbors ($Y_{\rm odd}$). This well known proton even-odd staggering is quantified in a global way as $G_{eo} = (\sum Y_{\rm even} - \sum Y_{\rm odd})/(\sum Y_{\rm even} + \sum Y_{\rm odd})$. For compound nuclei produced with higher excitation energy, the influence of the pairing correlation is gradually washed out, and thus the even-odd staggering decreases. This is illustrated in Table II, which also reports on the global proton even-odd effect measured for the thermal neutron-induced fission of ^{235}U [32]. In the latter case, where an excitation energy of 6.5 MeV (the neutron binding energy) is added to the system, the G_{eo} value is 2.5 times larger than that obtained in our data.

Previous data (Fig. 12(a) and Table II, [19]) also measured at GSI in inverse kinematics, exhibit a lower even-odd staggering and an increase of yields in the symmetric-fission valley. In the previous experiment, a selection in $B\rho$ was performed to maximize the number of measured electromagnetically induced fission events. Since only one fragment was identified for every fission event, it was not possible to unambiguously identify fission events that were caused purely by electromagnetic interactions. Therefore, fission following the abrasion of nucleons from the ^{238}U projectile was still partly included in the data, resulting in a higher mean excitation energy.

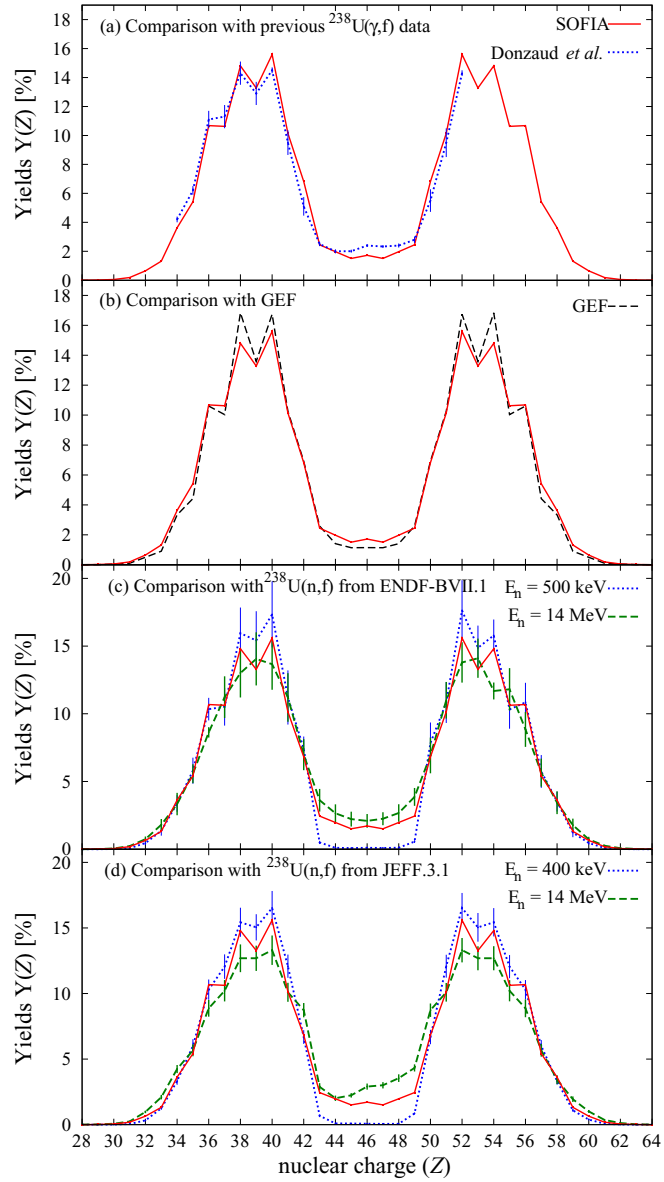

FIG. 12. Elemental yields of ^{238}U(γ,f) for this experiment (full red line) compared to (a) previous data [19] (dotted blue line), (b) results obtained with the GEF code [22] (dashed black line), (c) ^{238}U(n,f) evaluated data from ENDF-BVII.1 [31] at neutron-incident energies of 14 MeV (dashed green line) and 500 keV (dotted blue line), and (d) ^{238}U(n,f) evaluated data from JEFF.3.1 [29,30] at neutron-incident energies of 14 MeV (dashed green line) and 400 keV (dotted blue line).

The elemental yields obtained from the GEF code [22], using the calculated excitation function, give a satisfactory agreement with our measurement, with a slight underestimation of the symmetric splitting and an overestimate of the global proton even-odd staggering. The latter mainly comes from a much stronger local proton even-odd staggering (as defined

TABLE II. Global proton even-odd staggering for different data sets

Reaction	G_{eo} (%)
^{238}U(γ, f) SOFIA	10.12
^{238}U(γ, f) Donzaud *et al.* [19]	8.6
^{238}U(γ, f) GEF [22]	13.9
^{235}U(n_{th}, f) Lang *et al.* [32]	23.7
^{238}U($n_{500\,\mathrm{keV}}, f$) ENDF-BVII.1 [31]	11.31
^{238}U($n_{400\,\mathrm{keV}}, f$) JEFF.3.1 [29,30]	5.5
^{238}U($n_{14\,\mathrm{MeV}}, f$) ENDF-BVII.1 [31]	−0.7
^{238}U($n_{14\,\mathrm{MeV}}, f$) JEFF.3.1 [29,30]	5.6

in Ref. [33]) for asymmetric splits, whereas at symmetry and contrary to our data, the local even-odd staggering is fully washed out. This is highlighted in Fig. 13, which compares the local proton even-odd effect (δ_p) extracted from our data and the GEF results. Even if the amplitude in the fluctuation of δ_p around $Z = 50$ is well reproduced in the GEF calculations, its large value, which indicates a nuclear structure effect for this particular splitting, is quite underestimated. All these small discrepancies could indicate that the effect of the increase of the excitation energy is not fully reproduced by GEF.

Taking into account the neutron binding energy in ^{238}U, the mean excitation energy of 14.7 MeV corresponds to about 8.5 MeV incident-neutron energy for the ^{237}U(n, f) reaction. The comparison of the yields in the symmetric valley between our data and the ^{238}U(n, f) evaluation at two different neutron energies, 400 or 500 keV and 14 MeV [Figs. 12(c) and 12(d)], is compatible with this expected mean excitation energy. Even at this energy, our data show that the underlying structure effects influence the fission process. However, it seems that both evaluations underestimate the magnitude of the even-odd staggering, already at 400 and 500 keV, especially JEFF.3.1 [29,30]. At 14 MeV, the even-odd staggering given by JEFF.3.1 seems more reasonable that the one given by ENDF-BVII.1 [31] where odd-Z fragments are globally enhanced compared to even-Z fragments.

Finally, the statistical error bars obtained in the SOFIA experiment are reported in Fig. 12 and are, for some of them, smaller than the symbols. As one may check in Table IV, the highest relative statistical uncertainty is reached in the valley

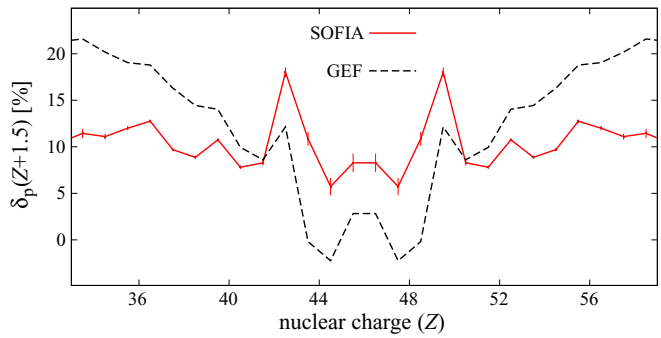

FIG. 13. Comparison of the local proton even-odd staggering, extracted from this data (full red line) and from the GEF calculations (dashed black line).

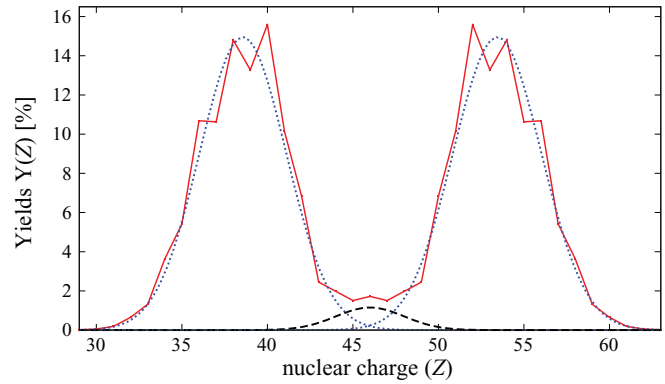

FIG. 14. Elemental yield distribution (full red line) fitted using a three-Gaussian distribution. The black dashed line corresponds to the fit of symmetric fission. Since elemental yields are asymmetric, the fits for the light and heavy groups (blue dotted lines) have the same parameters except for the mean values.

of symmetric fission events (<2%), or for very asymmetric splitting. For the most probable splits ($Z_1 = 40$, $Z_2 = 52$), they are as low as 0.3%. This is a strong improvement compared to previously existing data and the level of uncertainties in the evaluations.

B. Mean heavy charge

From the elemental yield distribution, it is possible to deduce the mean heavy charge using a fit with three Gaussian distributions: one for the light peak, one for symmetric fission, and the last one for the heavy peak. The latter provides the mean heavy charge, which is therefore discriminated from the symmetric component. Figure 14 exhibits the elemental yields with a full red line, fitted with these three Gaussian distributions. The asymmetric components are represented with dotted blue lines and the symmetric one with a dashed black line. The width of the symmetric component is not so well defined by these data, because the yields in the symmetric region are low. However, the mean heavy charge given by our fit, $\langle Z_H \rangle = 53.43 \pm 0.10$, is only weakly dependent on this feature, which is taken into account by the uncertainty attached to the value.

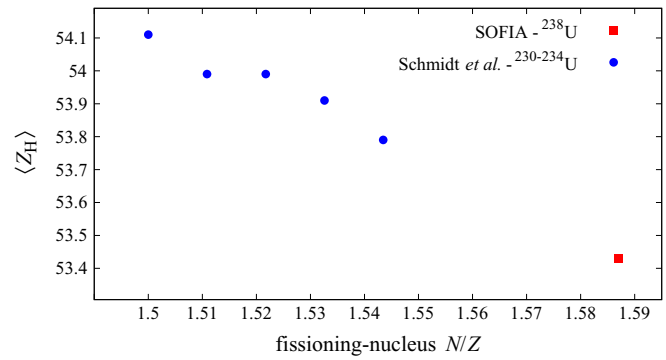

FIG. 15. Mean heavy charge depending on the Z/N ratio of the fissioning nucleus: the value for ^{238}U (this work, red square) is compared to data from Schmidt *et al.* [15] for uranium isotopes (blue circles).

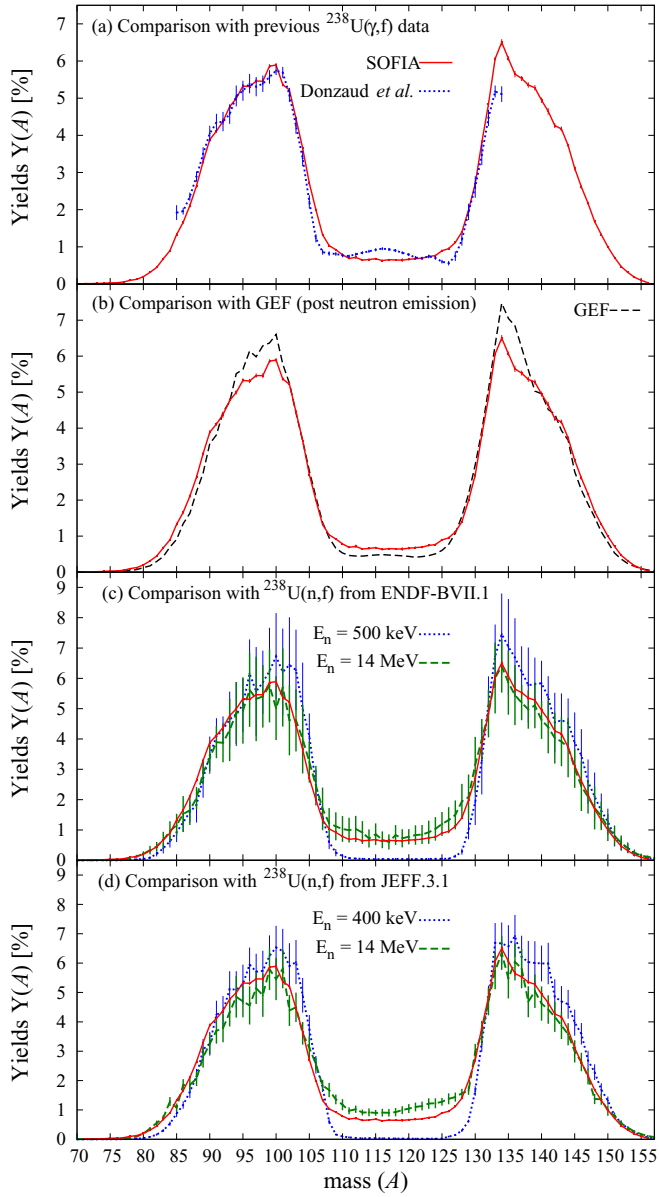

FIG. 16. Isobaric yields of ^{238}U(γ, f) for this experiment (full red line) compared to (a) previous data [19] (dotted blue line), (b) results obtained with the GEF code [22] (dashed black line), (c) ^{238}U(n, f) evaluated data from ENDF-BVII.1 [31] at neutron-incident energies of 14 MeV (dashed green line) and 500 keV (dotted blue line), and (d) ^{238}U(n, f) evaluated data from JEFF.3.1 [29,30] at neutron-incident energies of 14 MeV (dashed green line) and 400 keV (dotted blue line).

For different fissioning nuclei ($^{222–229}$Th, $^{224–232}$Pa, and $^{230–234}$U), it was previously found that the mean heavy charge is stable around $\langle Z_H \rangle = 54$ [15]. The previously measured values for $^{230–234}$U are reported in Fig. 15 and compared with our measurement for ^{238}U. For the uranium isotopic chain, the mean heavy charge value decreases slowly with increasing N/Z of the fissioning nucleus. This indicates an increasing influence of the so-called standard 1 (S1) fission mode for more neutron-rich nuclei as N/Z becomes closer to that of the doubly-magic ^{132}Sn. In the actinide region, the competition between three fission modes was previously suggested [34,35]. They correspond to different fission paths on the potential energy surface. Besides the S1 mode, characterized by a heavy fragment strongly influenced by the double magic ^{132}Sn nucleus, another asymmetric fission mode, the standard 2 (S2) mode, plays a major role. It is characterized by a heavy fragment around $A = 140$, possibly stabilized by the deformed neutron-shell gap at $N \sim 88$ [36]. Therefore, the S1 component increases for higher N/Z ratio, but the constant mean heavy charge around 54 and not around 50, shows the S2 mode is predominant in this uranium region. This confirms the conclusions drawn in Ref. [37]. Finally, the last fission mode, called superlong (SL), reflects symmetric fission and exhibits two highly deformed fission fragments at the scission configuration.

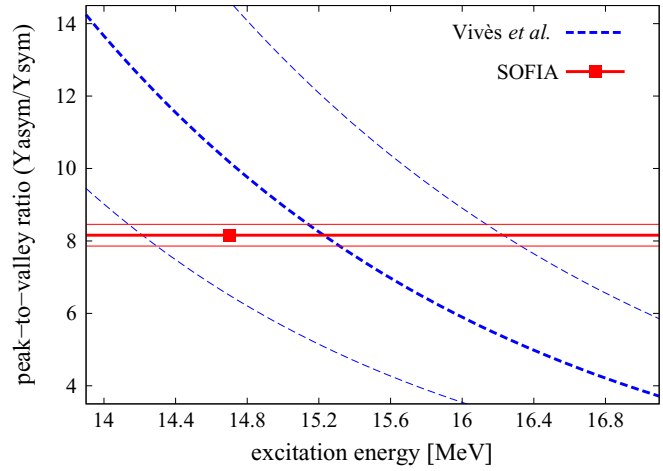

FIG. 17. Peak-to-valley ratio as function of excitation energy. The dashed blue lines correspond to the parametrization for the ^{238}U(n, f) reaction, with its uncertainties [38]. The SOFIA peak-to-valley ratio is plotted with error bars as full red lines and the calculated mean excitation energy is indicated as a red square.

C. Isobaric yields

Figure 16 shows the isobaric yields normalized to 200%, measured after prompt neutron emission, with their statistical uncertainties. As the excitation energy increases, the SL mode becomes more and more important. The peak-to-valley ratio, between asymmetric mass yields and symmetric mass yields, has been parametrized as function of the excitation energy for ^{238}U(n, f) in Ref. [38]. The comparison of our experimental value with this parametrization is represented in Fig. 17 and results in a mean excitation energy of 15.2 ± 1 MeV. This value, even if given for a ^{239}U compound nucleus, is fully compatible with the calculated mean excitation energy of 14.7 MeV also plotted in Fig. 17.

Figure 16(a) supports the argument made above that the previous experiment at the FRS [19] selected partly fragmentation-fission reactions resulting in higher excitation energies. Indeed, even if the comparison is reasonably satisfactory, the symmetric mode is more important than in our data.

The JEFF.3.1 [29,30] and ENDF-BVII.1 [31] evaluations at a neutron energy of 14 MeV [dashed green lines in Figs. 16(c)

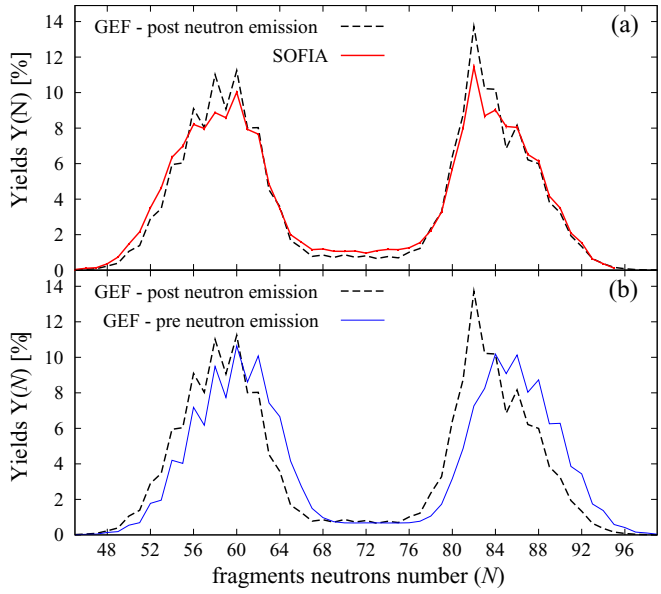

FIG. 18. Isotonic yields of ^{238}U(γ, f) obtained in this experiment [(a), full red line] and with the GEF code [22] after neutron emission [(a) and (b), dashed black line] and before neutron emission [(b), full blue line].

and 16(d)], are slightly shifted to heavier masses in the light group and match our experimental data for the heavy group. This tiny difference in mass in the light group is understood as a difference in mass in the compound nucleus (^{238}U in our case and ^{239}U in the evaluated data). All evaluated data, as well as the GEF calculations [dashed black line in Fig. 16(b)] agree with the enhancement of $A = 134$, which mainly comes from the favored population of $N = 82$ (as shown in the next section) coupled with the most probable split in nuclear charge ($Z_1 = 40$, $Z_2 = 52$).

D. Isotonic yields

Figure 18(a) clearly demonstrates an enhanced production of $N = 82$ isotones in our measurement (full red line). In this figure, the comparison with the neutron yields calculated by GEF [22] after neutron emission is given (dashed black line). The increased population of $N = 82$, well reproduced by GEF, can be attributed to the large spherical shell gap and its impact on the deexcitation of the heavy fission fragment. Indeed, the comparison of the pre- and post-neutron emission yields, given by GEF [Fig. 18(b)], indicates that this gap reduces the neutron emission from fragments reaching the $N = 82$ shell after some prompt neutron emission. For these isotones

TABLE III. Global neutron even-odd staggering after prompt neutron emission, for different data sets.

Reaction	G_{eo} (%)
^{238}U(γ, f) SOFIA	5.25
^{238}U(γ, f) GEF [22]	10.6
^{235}U(n_{th}, f) Lang *et al.* [32]	5.4

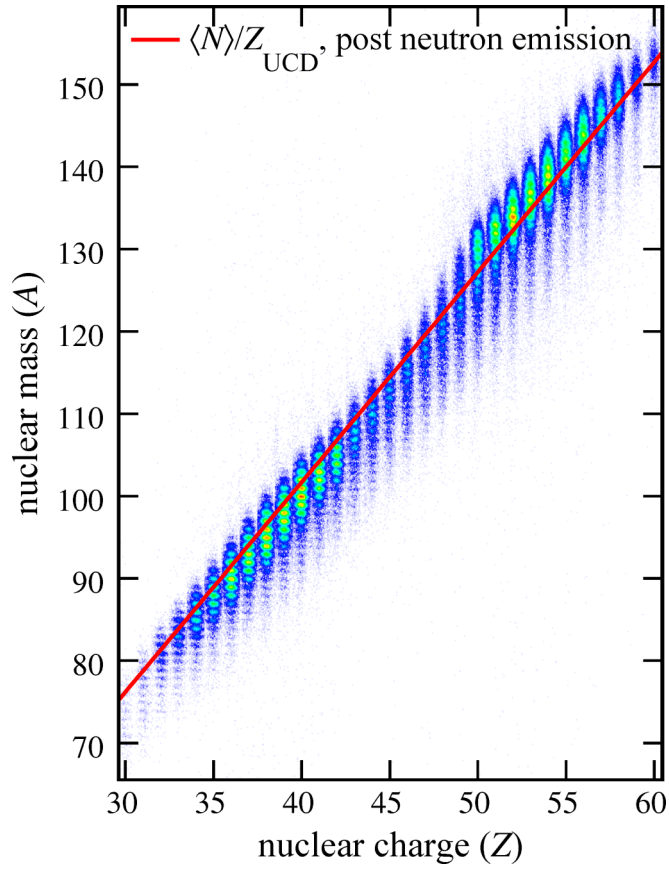

FIG. 19. Isotopic distribution of the fission fragments of ^{238}U obtained in this experiment for $Z_{sum} = 92$, before the nuclear subtraction. It illustrates the resolution reached for the whole fission-fragment range. The red line indicates the unchanged charge density hypothesis after prompt neutron evaporation. See text for details.

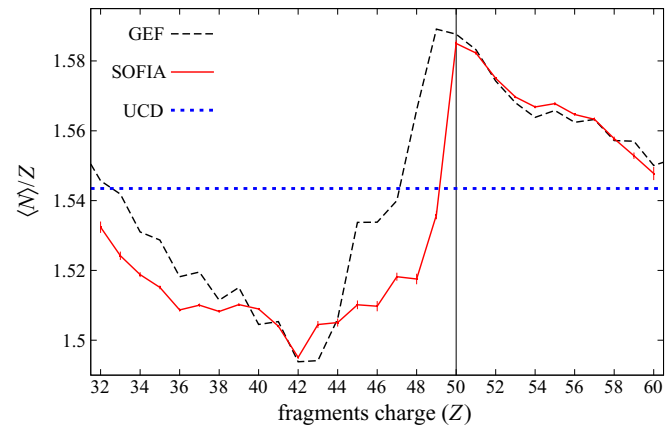

FIG. 20. Polarization of the fission fragments after the prompt neutron emission, depending on their nuclear charge obtained for this work (full red line), compared with results from GEF (dashed black line [22]). The unchanged charge density hypothesis after prompt neutron evaporation is reported by the thick dashed blue line. The vertical line indicates the $Z = 50$ magic number.

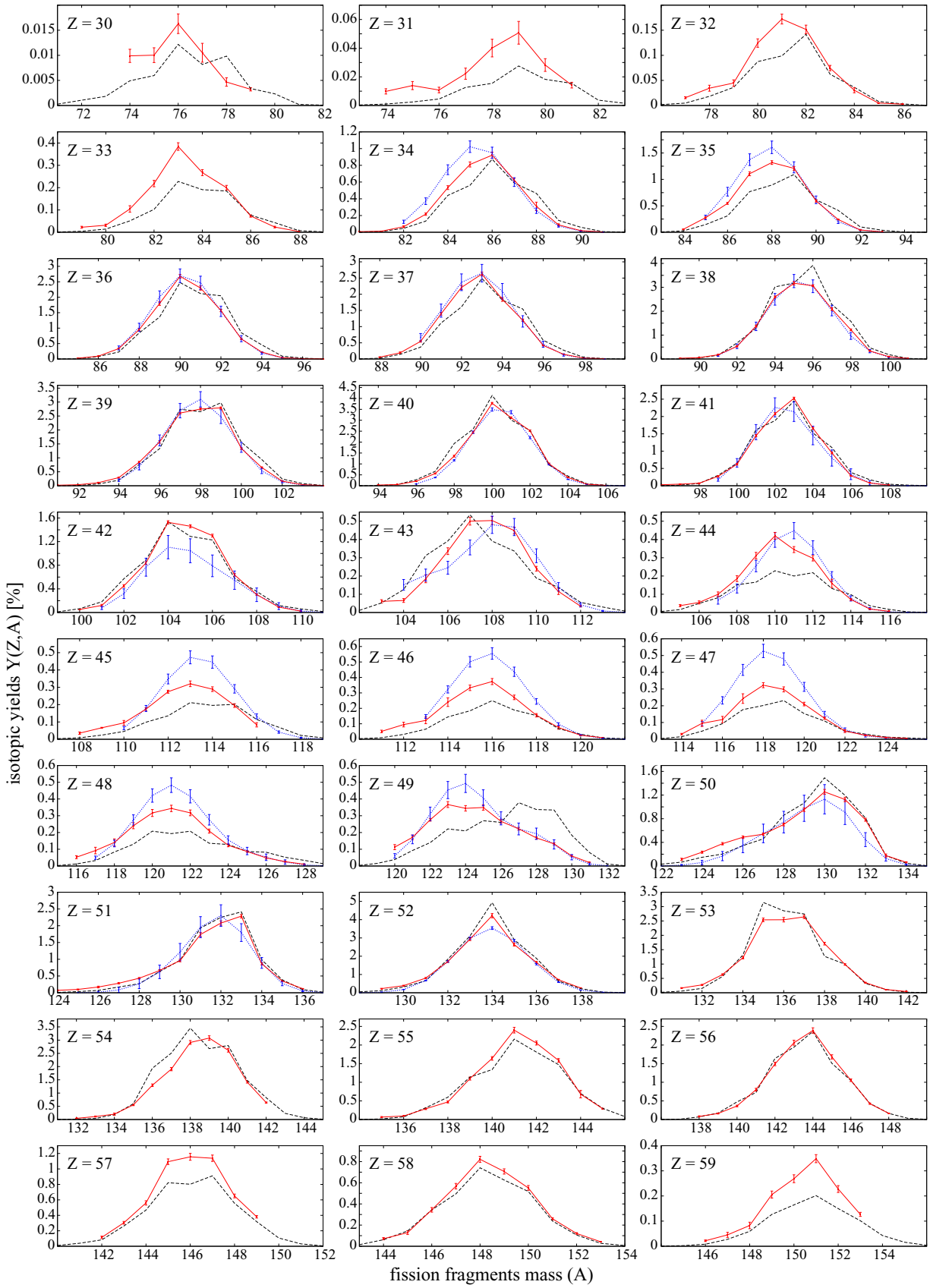

FIG. 21. Isotopic yields of electromagnetically induced fission of ^{238}U obtained in this work (full red line), compared with data obtained from a previous experiment (dotted blue line [19]) and GEF (dashed black line [22]).

the excitation energy of the heavy fragment is below their neutron separation energy. This gap acts therefore as a trap in the neutron evaporation phase. Moreover, whereas the global proton even-odd staggering measured in fission at very low excitation energies is much higher than in our data (Table II, Sec. IV A), the opposite is the case for the global neutron even-odd staggering, where both values are similar (Table III). This establishes that the global neutron even-odd effect is essentially governed by neutron evaporation rather than by the value of the excitation energy.

Again, the comparison between GEF and our data is satisfactory. The shape of the neutron-yields distributions [Fig. 18(a)] are similar but the neutron even-odd staggering (see also Table III) and the peak-over-valley ratio are overestimated in the calculation.

E. Isotopic yields

Figure 19 shows the isotopic distribution (A_{FF} vs Z_{FF}) obtained in this experiment. A superimposed red line indicates the unchanged charge density (UCD) hypothesis. In this scenario, the mass-over-charge ratio for all fission fragments is considered to be equal to that of the fissioning nucleus. Since our results give a mean total neutron multiplicity of about 4.3 ± 0.5, the UCD line is thus calculated, taking into account, as a first approximation, a total evaporation of four neutrons by the fission fragments.

Fission fragments from $Z = 30$ up to $Z = 49$ stand below this UCD line, whereas those whose nuclear charge is higher than $Z = 50$ are above. Therefore, this hypothesis is valid only as a first approximation, and this sudden change signs a sharp transition in the polarization (or neutron excess, defined as $\langle N \rangle / Z$) of the fission fragments, as first observed in the fission of ^{240}Pu [16,39]. This is clearly illustrated in Fig. 20, which shows the polarization of the fission fragments as a function of the nuclear charge for our data (red full line) and for the results obtained from GEF (black dotted line [22]). GEF calculations reproduce well the shape and the values of the polarization distribution especially for the heavier fragments, with a discrepancy in the location of the transition, predicted to happen at one charge lighter. The behavior of the neutron excess can be understood by looking at the isotopic yields.

The isotopic yields obtained in this experiment are represented with the full red lines in Fig. 21. For every element, except 49 and 50, the isotopic yields exhibit a Gaussian-like distribution. For $Z = 49$ and $Z = 50$, the isotopic yields distributions are clearly asymmetric. This corresponds precisely to the change in polarization, already illustrated in Figs. 19 and 20. Indeed, the isotopic distribution of those specific yields, highlighted in Fig. 22, has two components, obtained using a two-Gaussian fit, whose contribution changes from $Z = 49$ to $Z = 50$. For $Z = 49$, fission is follows mainly the SL symmetric mode, whereas for $Z = 50$ the S1 asymmetric mode dominates. In this latter case, the Gaussian fit of the S1 mode is centered around $N = 80 \pm 0.5$. Taking into account, as a first approximation, an evaporation of two neutrons by the heavy fragment, a mean value of $N = 82$ is found for the S1 mode before the prompt neutron emission. As previously mentioned, this change of polarization is expected by the GEF code to happen already at $Z = 49$, where the isotopic distribution is predicted to be more neutron-rich compared to this experiment.

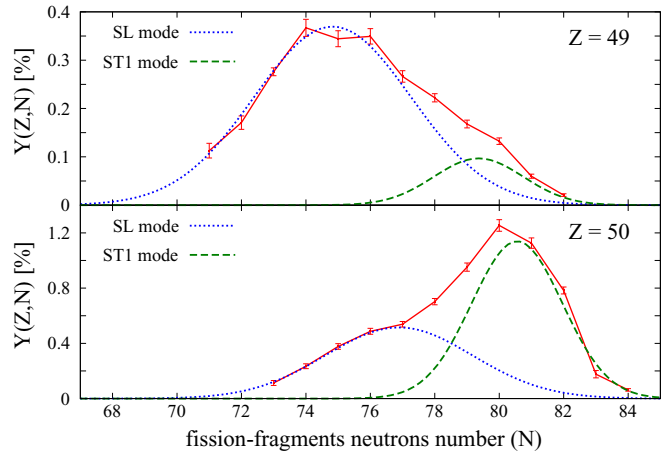

FIG. 22. Full red line: isotopic yields obtained for $Z = 49$ (up) and $Z = 50$ (down). Dotted blue line: contribution of the SL symmetric fission mode. Dashed green line: contribution of the S1 asymmetric fission mode. Both contributions are obtained using a two-Gaussian fit.

Interestingly, the competition between the two fission modes in the two asymmetric isotopic distributions testifies to the fact that the heavy fragment can undergo fission with two stable configurations: a very deformed configuration associated to the SL mode and a nearly spherical one associated with the S1 channel.

Despite this difference in the polarization change, the prediction by GEF of the isotopic yields (dashed black line in Fig. 21) is excellent, especially for the most probable asymmetric splits, from $Z = 36$ to $Z = 42$ in the light group and from $Z = 50$ even up to $Z = 58$ in the heavy group.

The isotopic yields between our results and previous experimental data (dotted blue line in Fig. 21 [19]) agree quite well for the light fragment group, and discrepancies are observed only for symmetric fission. Indeed, the weight of the fragmentation-fission reactions, not fully removed in Ref. [19], is higher in the symmetric valley, as can be seen in the comparison of the elemental distributions between electromagnetic induced fission [Fig. 9(b)] and fragmentation-fission reactions [thick pink line in Fig. 9(a)].

V. CONCLUSION

Within the SOFIA Collaboration, an experimental setup has been developed around the ALADIN magnet, forming a high-resolution magnetic spectrometer, to identify the mass and charge of both fission fragments in coincidence. Low-energy fission events are induced by electromagnetic excitation of relativistic beams, in inverse kinematics. In this publication, we focus on the study of the fission of ^{238}U. This reaction can be seen as a surrogate reaction to ^{237}U(n, f), leading to a ^{238}U compound nucleus excited at 14.7 MeV on average, but with a tail in excitation energy up to 30 MeV approximately.

The experimental breakthrough here is the ability to detect and identify both fission fragments in coincidence in terms

of their nuclear charge and mass, without any ambiguities. The fission-fragment distributions are obtained with a good resolution for all fission fragments, and it was possible to extract low-energy Coulomb fission events.

This experiment provides new high-resolution data on the elemental, isobaric, isotonic, and isotopic yields. The precision obtained in this experiment is relevant for applications, and provides new information on the impact of nuclear structure on the nuclear-fission process. Our data emphasize the growing importance of the asymmetric S1 fission mode for uranium fissioning nuclei having a higher N/Z ratio, even if the S2 mode remains predominant. This is supported by an enhanced probability of producing heavy fission fragments with a mean charge $\langle Z_H \rangle = 53.43$, a bit smaller compared to what has been measured for fission of lighter uranium isotopes, for which $\langle Z_H \rangle$ is closer to 54. Then, the increased production of $N = 82$ fission fragments seems to be an effect of the influence of the strong spherical neutron shell gap on the deexcitation of the fission fragments by neutron evaporation.

The comparison with the GEF model, which allows us to take the calculated excitation functions as input, is excellent, especially for measured isotopic yields. Still there are significant discrepancies related to the even-odd staggering and the production of fission fragments in the symmetric valley. These deviations will allow us to improve GEF substantially and will certainly lead to a better general quantitative description of the fission quantities for systems close to ^{238}U.

Finally, these new data, of unprecedent accuracy, are in complete agreement with previous measurements on electromagnetically induced fission of ^{238}U, and also with neutron-induced fission of ^{235,238}U. The differences between the different data sets are understood. This agreement validates our experimental approach and our results not only for ^{238}U, reported in this article, but also for data on other actinides and pre-actinides, which will be reported at a later time.

ACKNOWLEDGMENTS

We thank P. Romain (from CEA, DAM, DIF) for performing the TALYS calculations providing fission probabilities as function of the excitation energy. This work was supported by the GSI/IN2P3-CNRS collaboration agreement 04-48. E.C. is supported by the Spanish Ministry project FPA2010-22174-C02. J.L.R.S. also acknowledges the support of the European Commission under Project ANDES-FP7-249671. We would like to thank the CEA's nuclear energy division for its financial support.

APPENDIX: NUMERICAL VALUES

All the values given in the following tables are listed with their statistical errors. As explained in the introduction of Sec. IV, the systematic uncertainties should be added to the results. All yields are measured after the prompt neutron emission. Concerning the elemental yields, since both fission fragments are detected, the results have been symmetrized.

TABLE IV. Elemental yields normalized to 200%.

Z_l, Z_H	$Y(Z)$ (%)	Z_l, Z_H	$Y(Z)$ (%)
29,63	0.017 ± 0.003	30,62	0.051 ± 0.005
31,61	0.188 ± 0.007	32,60	0.649 ± 0.011
33,59	1.317 ± 0.015	34,58	3.627 ± 0.022
35,57	5.419 ± 0.027	36,56	10.681 ± 0.035
37,55	10.627 ± 0.036	38,54	14.802 ± 0.043
39,53	13.277 ± 0.042	40,52	15.592 ± 0.045
41,51	10.141 ± 0.040	42,50	6.822 ± 0.037
43,49	2.447 ± 0.029	44,48	1.976 ± 0.029
45,47	1.508 ± 0.029	46,46	1.718 ± 0.029

TABLE V. Isobaric yields normalized to 200%.

A	$Y(A)$ (%)	A	$Y(A)$ (%)
71	0.012 ± 0.002	72	0.011 ± 0.002
73	0.014 ± 0.002	74	0.018 ± 0.002
75	0.032 ± 0.004	76	0.032 ± 0.004
77	0.054 ± 0.007	78	0.098 ± 0.007
79	0.126 ± 0.010	80	0.198 ± 0.011
81	0.313 ± 0.017	82	0.447 ± 0.018
83	0.676 ± 0.030	84	0.897 ± 0.025
85	1.330 ± 0.042	86	1.659 ± 0.045
87	2.107 ± 0.050	88	2.641 ± 0.055
89	3.289 ± 0.050	90	3.886 ± 0.060
91	4.113 ± 0.048	92	4.377 ± 0.084
93	4.772 ± 0.056	94	4.992 ± 0.056
95	5.327 ± 0.058	96	5.309 ± 0.060
97	5.462 ± 0.061	98	5.458 ± 0.067
99	5.862 ± 0.054	100	5.892 ± 0.057
101	5.367 ± 0.053	102	5.221 ± 0.052
103	4.454 ± 0.051	104	3.655 ± 0.042
105	2.712 ± 0.053	106	1.997 ± 0.032
107	1.325 ± 0.031	108	1.034 ± 0.028
109	0.922 ± 0.024	110	0.787 ± 0.026
111	0.687 ± 0.024	112	0.716 ± 0.046
113	0.643 ± 0.027	114	0.659 ± 0.032
115	0.681 ± 0.024	116	0.630 ± 0.027
117	0.653 ± 0.023	118	0.646 ± 0.025
119	0.642 ± 0.051	120	0.664 ± 0.038
121	0.680 ± 0.035	122	0.695 ± 0.034
123	0.742 ± 0.028	124	0.764 ± 0.029
125	0.895 ± 0.031	126	0.951 ± 0.033
127	1.118 ± 0.026	128	1.397 ± 0.030
129	1.992 ± 0.042	130	2.697 ± 0.062
131	3.810 ± 0.055	132	4.835 ± 0.070
133	6.062 ± 0.050	134	6.501 ± 0.087
135	6.068 ± 0.061	136	5.648 ± 0.090
137	5.530 ± 0.068	138	5.356 ± 0.072
139	5.279 ± 0.074	140	4.947 ± 0.071
141	4.647 ± 0.088	142	4.265 ± 0.067
143	4.172 ± 0.065	144	3.728 ± 0.046
145	3.112 ± 0.056	146	2.614 ± 0.047
147	2.171 ± 0.041	148	1.681 ± 0.036
149	1.329 ± 0.029	150	1.000 ± 0.026
151	0.714 ± 0.022	152	0.468 ± 0.023
153	0.314 ± 0.013	154	0.183 ± 0.010
155	0.101 ± 0.006	156	0.036 ± 0.004

TABLE VI. Isotonic yields normalized to 200%.

N	$Y(N)$ (%)	N	$Y(N)$ (%)
43	0.010 ± 0.002	44	0.023 ± 0.004
45	0.037 ± 0.004	46	0.104 ± 0.009
47	0.142 ± 0.011	48	0.359 ± 0.023
49	0.738 ± 0.025	50	1.475 ± 0.037
51	2.157 ± 0.044	52	3.517 ± 0.072
53	4.635 ± 0.080	54	6.354 ± 0.102
55	6.983 ± 0.110	56	8.208 ± 0.090
57	7.977 ± 0.111	58	8.872 ± 0.080
59	8.581 ± 0.083	60	10.019 ± 0.076
61	7.929 ± 0.066	62	7.663 ± 0.066
63	4.844 ± 0.059	64	3.467 ± 0.049
65	2.002 ± 0.042	66	1.577 ± 0.036
67	1.159 ± 0.033	68	1.189 ± 0.046
69	1.067 ± 0.044	70	1.059 ± 0.044
71	1.074 ± 0.035	72	0.960 ± 0.032
73	1.096 ± 0.035	74	1.168 ± 0.034
75	1.156 ± 0.040	76	1.261 ± 0.034
77	1.553 ± 0.038	78	2.231 ± 0.049
79	3.280 ± 0.065	80	5.714 ± 0.105
81	8.016 ± 0.119	82	11.433 ± 0.153
83	8.689 ± 0.136	84	9.013 ± 0.118
85	8.094 ± 0.118	86	8.038 ± 0.115
87	6.517 ± 0.099	88	6.138 ± 0.100
89	4.170 ± 0.126	90	3.501 ± 0.064
91	2.095 ± 0.043	92	1.549 ± 0.034
93	0.632 ± 0.020	94	0.364 ± 0.015
95	0.113 ± 0.016		

TABLE VII. Isotopic yields normalised to 200%.

Z	A	$Y(Z,A)$ (%)	Z	A	$Y(Z,A)$ (%)
30	74	0.010 ± 0.002	30	75	0.010 ± 0.002
30	76	0.016 ± 0.002	30	77	0.011 ± 0.002
30	78	0.005 ± 0.001	30	79	0.003 ± 0.001
31	74	0.010 ± 0.002	31	75	0.014 ± 0.003
31	76	0.011 ± 0.002	31	77	0.022 ± 0.004
31	78	0.040 ± 0.007	31	79	0.051 ± 0.008
31	80	0.028 ± 0.005	31	81	0.014 ± 0.002
32	77	0.016 ± 0.002	32	78	0.035 ± 0.006
32	79	0.045 ± 0.007	32	80	0.124 ± 0.009
32	81	0.172 ± 0.010	32	82	0.152 ± 0.009
32	83	0.075 ± 0.006	32	84	0.030 ± 0.006
32	85	0.005 ± 0.001	32	86	0.003 ± 0.001
33	79	0.023 ± 0.005	33	80	0.031 ± 0.006
33	81	0.104 ± 0.015	33	82	0.218 ± 0.015
33	83	0.384 ± 0.017	33	84	0.267 ± 0.014
33	85	0.200 ± 0.011	33	86	0.073 ± 0.006
33	87	0.023 ± 0.004	33	88	0.003 ± 0.001
34	80	0.008 ± 0.002	34	81	0.013 ± 0.002
34	82	0.066 ± 0.012	34	83	0.216 ± 0.015
34	84	0.534 ± 0.024	34	85	0.810 ± 0.031
34	86	0.921 ± 0.037	34	87	0.625 ± 0.021
34	88	0.310 ± 0.050	34	89	0.088 ± 0.014
34	90	0.020 ± 0.003	34	91	0.003 ± 0.001
35	84	0.056 ± 0.008	35	85	0.274 ± 0.017
35	86	0.547 ± 0.019	35	87	1.107 ± 0.038
35	88	1.319 ± 0.036	35	89	1.209 ± 0.036
35	90	0.593 ± 0.022	35	91	0.241 ± 0.008
35	92	0.043 ± 0.006	35	93	0.008 ± 0.002
36	85	0.028 ± 0.005	36	86	0.091 ± 0.013
36	87	0.338 ± 0.018	36	88	0.952 ± 0.035
36	89	1.799 ± 0.062	36	90	2.677 ± 0.063
36	91	2.298 ± 0.069	36	92	1.571 ± 0.040
36	93	0.648 ± 0.022	36	94	0.224 ± 0.011
36	95	0.041 ± 0.006	36	96	0.010 ± 0.002
36	97	0.006 ± 0.002	37	88	0.058 ± 0.008
37	89	0.191 ± 0.028	37	90	0.545 ± 0.025
37	91	1.395 ± 0.040	37	92	2.210 ± 0.066
37	93	2.624 ± 0.061	37	94	1.842 ± 0.061
37	95	1.199 ± 0.037	37	96	0.420 ± 0.017
37	97	0.145 ± 0.007	37	98	0.027 ± 0.004
37	99	0.011 ± 0.002	38	89	0.032 ± 0.007
38	90	0.057 ± 0.010	38	91	0.175 ± 0.014
38	92	0.531 ± 0.026	38	93	1.375 ± 0.044
38	94	2.597 ± 0.037	38	95	3.170 ± 0.073
38	96	3.067 ± 0.039	38	97	2.090 ± 0.055
38	98	1.222 ± 0.037	38	99	0.334 ± 0.015
38	100	0.100 ± 0.018	38	101	0.020 ± 0.004
39	91	0.020 ± 0.003	39	92	0.037 ± 0.007
39	93	0.110 ± 0.017	39	94	0.291 ± 0.019
39	95	0.844 ± 0.033	39	96	1.572 ± 0.044
39	97	2.605 ± 0.035	39	98	2.751 ± 0.035
39	99	2.792 ± 0.035	39	100	1.336 ± 0.032
39	101	0.656 ± 0.023	39	102	0.166 ± 0.023
39	103	0.037 ± 0.007	39	104	0.010 ± 0.003
40	94	0.033 ± 0.007	40	95	0.054 ± 0.009
40	96	0.210 ± 0.016	40	97	0.561 ± 0.026
40	98	1.358 ± 0.040	40	99	2.442 ± 0.036
40	100	3.779 ± 0.041	40	101	3.118 ± 0.037
40	102	2.520 ± 0.033	40	103	1.010 ± 0.031
40	104	0.381 ± 0.017	40	105	0.071 ± 0.006
40	106	0.018 ± 0.004	41	94	0.019 ± 0.004
41	95	0.020 ± 0.004	41	96	0.030 ± 0.006
41	97	0.047 ± 0.009	41	98	0.073 ± 0.012
41	99	0.272 ± 0.022	41	100	0.624 ± 0.026
41	101	1.448 ± 0.029	41	102	2.079 ± 0.031
41	103	2.526 ± 0.032	41	104	1.659 ± 0.026
41	105	0.949 ± 0.027	41	106	0.290 ± 0.011
41	107	0.080 ± 0.006	41	108	0.017 ± 0.003
42	100	0.052 ± 0.006	42	101	0.120 ± 0.018
42	102	0.450 ± 0.022	42	103	0.839 ± 0.025
42	104	1.526 ± 0.028	42	105	1.460 ± 0.027
42	106	1.302 ± 0.025	42	107	0.637 ± 0.022
42	108	0.305 ± 0.014	42	109	0.091 ± 0.006
42	110	0.023 ± 0.004	43	103	0.061 ± 0.010
43	104	0.066 ± 0.011	43	105	0.185 ± 0.022
43	106	0.336 ± 0.019	43	107	0.500 ± 0.022
43	108	0.504 ± 0.022	43	109	0.449 ± 0.019
43	110	0.240 ± 0.013	43	111	0.115 ± 0.017
43	112	0.034 ± 0.005	44	105	0.038 ± 0.006
44	106	0.055 ± 0.009	44	107	0.100 ± 0.013
44	108	0.186 ± 0.016	44	109	0.311 ± 0.018
44	110	0.420 ± 0.019	44	111	0.345 ± 0.017
44	112	0.297 ± 0.015	44	113	0.159 ± 0.023
44	114	0.071 ± 0.005	44	115	0.019 ± 0.003

TABLE VII. (*Continued.*)

Z	A	$Y(Z,A)$ (%)	Z	A	$Y(Z,A)$ (%)
44	116	0.007 ± 0.001	45	108	0.035 ± 0.007
45	109	0.066 ± 0.003	45	110	0.094 ± 0.015
45	111	0.174 ± 0.008	45	112	0.274 ± 0.009
45	113	0.320 ± 0.017	45	114	0.289 ± 0.014
45	115	0.195 ± 0.011	45	116	0.083 ± 0.013
46	111	0.051 ± 0.009	46	112	0.095 ± 0.016
46	113	0.122 ± 0.022	46	114	0.240 ± 0.028
46	115	0.333 ± 0.018	46	116	0.373 ± 0.020
46	117	0.271 ± 0.015	46	118	0.155 ± 0.012
46	119	0.076 ± 0.012	46	120	0.026 ± 0.003
46	121	0.010 ± 0.002	47	114	0.031 ± 0.005
47	115	0.095 ± 0.019	47	116	0.118 ± 0.019
47	117	0.243 ± 0.029	47	118	0.323 ± 0.016
47	119	0.298 ± 0.016	47	120	0.210 ± 0.011
47	121	0.125 ± 0.008	47	122	0.049 ± 0.009
47	123	0.024 ± 0.004	47	124	0.011 ± 0.002
47	125	0.005 ± 0.002	48	116	0.053 ± 0.010
48	117	0.092 ± 0.020	48	118	0.141 ± 0.022
48	119	0.240 ± 0.019	48	120	0.317 ± 0.021
48	121	0.344 ± 0.019	48	122	0.317 ± 0.018
48	123	0.209 ± 0.013	48	124	0.124 ± 0.009
48	125	0.087 ± 0.006	48	126	0.049 ± 0.008
48	127	0.026 ± 0.004	48	128	0.011 ± 0.002
49	120	0.113 ± 0.016	49	121	0.171 ± 0.014
49	122	0.276 ± 0.009	49	123	0.367 ± 0.018
49	124	0.344 ± 0.017	49	125	0.349 ± 0.017
49	126	0.266 ± 0.012	49	127	0.222 ± 0.009
49	128	0.168 ± 0.009	49	129	0.132 ± 0.007
49	130	0.060 ± 0.005	49	131	0.021 ± 0.003
50	123	0.113 ± 0.018	50	124	0.234 ± 0.018
50	125	0.377 ± 0.021	50	126	0.487 ± 0.022
50	127	0.538 ± 0.021	50	128	0.702 ± 0.023
50	129	0.952 ± 0.030	50	130	1.254 ± 0.042
50	131	1.126 ± 0.038	50	132	0.783 ± 0.026
50	133	0.177 ± 0.027	50	134	0.063 ± 0.010
51	124	0.072 ± 0.015	51	125	0.100 ± 0.012
51	126	0.171 ± 0.026	51	127	0.284 ± 0.019
51	128	0.434 ± 0.023	51	129	0.663 ± 0.031
51	130	0.961 ± 0.037	51	131	1.741 ± 0.061
51	132	2.081 ± 0.066	51	133	2.286 ± 0.054
51	134	0.865 ± 0.032	51	135	0.352 ± 0.018

TABLE VII. (*Continued.*)

Z	A	$Y(Z,A)$ (%)	Z	A	$Y(Z,A)$ (%)
51	136	0.123 ± 0.005	52	129	0.226 ± 0.019
52	130	0.390 ± 0.024	52	131	0.803 ± 0.035
52	132	1.708 ± 0.053	52	133	2.934 ± 0.078
52	134	4.220 ± 0.117	52	135	2.638 ± 0.081
52	136	1.661 ± 0.055	52	137	0.712 ± 0.026
52	138	0.264 ± 0.013	53	131	0.167 ± 0.013
53	132	0.275 ± 0.018	53	133	0.634 ± 0.028
53	134	1.220 ± 0.039	53	135	2.539 ± 0.062
53	136	2.543 ± 0.077	53	137	2.642 ± 0.059
53	138	1.711 ± 0.048	53	139	0.985 ± 0.028
53	140	0.352 ± 0.014	53	141	0.113 ± 0.006
53	142	0.044 ± 0.010	54	132	0.044 ± 0.006
54	133	0.113 ± 0.020	54	134	0.201 ± 0.044
54	135	0.554 ± 0.030	54	136	1.295 ± 0.049
54	137	1.904 ± 0.062	54	138	2.912 ± 0.073
54	139	3.077 ± 0.086	54	140	2.614 ± 0.066
54	141	1.416 ± 0.039	54	142	0.642 ± 0.023
55	135	0.065 ± 0.015	55	136	0.094 ± 0.011
55	137	0.288 ± 0.022	55	138	0.471 ± 0.028
55	139	1.100 ± 0.042	55	140	1.641 ± 0.049
55	141	2.398 ± 0.076	55	142	2.053 ± 0.053
55	143	1.588 ± 0.049	55	144	0.681 ± 0.101
55	145	0.289 ± 0.015	56	138	0.083 ± 0.016
56	139	0.162 ± 0.014	56	140	0.364 ± 0.022
56	141	0.801 ± 0.036	56	142	1.492 ± 0.047
56	143	2.062 ± 0.067	56	144	2.390 ± 0.073
56	145	1.682 ± 0.056	56	146	1.055 ± 0.035
56	147	0.426 ± 0.019	56	148	0.167 ± 0.006
57	142	0.115 ± 0.016	57	143	0.304 ± 0.018
57	144	0.560 ± 0.028	57	145	1.093 ± 0.036
57	146	1.156 ± 0.045	57	147	1.138 ± 0.041
57	148	0.650 ± 0.025	57	149	0.381 ± 0.016
58	144	0.072 ± 0.011	58	145	0.129 ± 0.018
58	146	0.344 ± 0.022	58	147	0.568 ± 0.026
58	148	0.822 ± 0.029	58	149	0.707 ± 0.025
58	150	0.551 ± 0.023	58	151	0.260 ± 0.010
58	152	0.121 ± 0.008	58	153	0.043 ± 0.003
59	146	0.022 ± 0.004	59	147	0.045 ± 0.010
59	148	0.083 ± 0.013	59	149	0.206 ± 0.014
59	150	0.269 ± 0.016	59	151	0.348 ± 0.016
59	152	0.228 ± 0.014	59	153	0.127 ± 0.008

[1] https://www-nds.iaea.org/exfor/endf.htm
[2] G. Siegert *et al.*, Phys. Lett. B **53**, 45 (1974).
[3] H.G. Clerc *et al.*, Nucl. Instrum. Methods **124**, 607 (1975).
[4] U. Quade *et al.*, Nucl. Instrum. Methods **164**, 435 (1979).
[5] K. Meierbachtol *et al.*, Nucl. Instrum. Methods Phys. Res., Sect. A **788**, 59 (2015).
[6] M. O. Frégeau *et al.*, Nucl. Instrum. Methods Phys. Res., Sect. A **817**, 35 (2016).
[7] D. Dore *et al.*, Eur. Phys. J. Web Conf **62**, 05005 (2013).
[8] A. Oed *et al.*, Nucl. Instrum. Methods **219**, 569 (1984).
[9] E. Moll *et al.*, Nucl. Instrum. Methods **123**, 615 (1975).
[10] G. Diiorio and B.W. Wehring, Nucl. Instrum. Methods **147**, 487 (1977).
[11] D. Rochman *et al.*, Nucl. Phys. A **710**, 3 (2002).
[12] A. Bail, O. Serot, L. Mathieu, O. Litaize, T. Materna, U. Koster, H. Faust, A. Letourneau, and S. Panebianco, Phys. Rev. C **84**, 034605 (2011).
[13] P. Armbruster *et al.*, Z. Phys. A **355**, 191 (1996).
[14] K.-H. Schmidt *et al.*, Phys. Lett. B **325**, 313 (1994).
[15] K.-H. Schmidt *et al.*, Nucl. Phys. A **665**, 221 (2000).
[16] M. Caamaño, O. Delaune *et al.*, Phys. Rev. C **88**, 024605 (2013).
[17] C. Rodríguez-Tajes *et al.*, Phys. Rev. C **89**, 024614 (2014).

[18] H. Geissel *et al.*, Nucl. Instrum. Methods Phys. Res., Sect. B **70**, 286 (1992).
[19] C. Donzaud *et al.*, Eur. Phys. J. A **1**, 407 (1998).
[20] J. T. Caldwell, E. J. Dowdy, B. L. Berman, R. A. Alvarez, and P. Meyer, Phys. Rev. C **21**, 1215 (1980).
[21] A. Koning, S. Hilaire, and M. Duijvestijn, in *Proceeding of the International Conference on Nuclear Data for Science and Technology - ND2007* (EDP Sciences, Paris, 2008), pp. 211–214.
[22] K.-H. Schmidt *et al.*, Nucl. Data Sheets **131**, 107 (2016).
[23] The ALADIN Collaboration, GSI Scientific Report 1988, GSI 89-1, 292 (1989).
[24] W. B. Christie *et al.*, Nucl. Instrum. Methods Phys. Res., Sect. A **255**, 466 (1987).
[25] ALICE collaboration, J. Phys. G: Nucl. Part. Phys. **30**, 1517 (2004).
[26] A. Ebran *et al.*, Nucl. Instrum. Methods Phys. Res., Sect. A **728**, 40 (2013).
[27] J. R. Cummings, W. R. Binns, T. L. Garrard, M. H. Israel, J. Klarmann, E. C. Stone, and C. J. Waddington, Phys. Rev. C **42**, 2530 (1990).
[28] http://www.khs-erzhausen.de/CONFID.html
[29] A. J. Koning *et al.*, JEFF Report 21, Nuclear Energy Agency, 2006 (unpublished).
[30] A. J. Koning *et al.*, JEFF Report 23, Nuclear Energy Agency, 2013 (unpublished).
[31] M. Chadwick *et al.*, Nucl. Data Sheets **112**, 2887 (2011).
[32] W. Lang *et al.*, Nucl. Phys. A **345**, 34 (1980).
[33] B. L. Tracy *et al.*, Phys. Rev. C **5**, 222 (1972).
[34] F.-J. Hambsch *et al.*, Nucl. Phys. A **491**, 56 (1989).
[35] U. Brosa *et al.*, Phys. Rep. **197**, 167 (1990).
[36] B. D. Wilkins, E. P. Steinberg, and R. R. Chasman, Phys. Rev. C **14**, 1832 (1976).
[37] C. Böckstiegel *et al.*, Nucl. Phys. A **802**, 12 (2008).
[38] F. Vives *et al.*, Nucl. Phys. A **662**, 63 (2000).
[39] M. Caamano, F. Farget, O. Delaune, K.H . Schmidt, C. Schmitt, L. Audouin, C. O. Bacri, J. Benlliure, E. Casarejos, X. Derkx, B. Fernandez-Dominguez, L. Gaudefroy, C. Golabek, B. Jurado, A. Lemasson, D. Ramos, C. Rodriguez-Tajes, T. Roger, and A. Shrivastava, Phys. Rev. C **92**, 034606 (2015).